Design of Multi-Mode Linear Electric Machine for Charging and Propulsion of Vacuum Tube Train

Dong, Jianning; Becetti, Belkassem; Bauer, Pavol

DOI
10.1109/ICEM51905.2022.9910702

Publication date
2022

Document Version
Final published version

Published in
Proceedings of the 2022 International Conference on Electrical Machines (ICEM)

Design of Multi-Mode Linear Electric Machine for Charging and Propulsion of Vacuum Tube Train

Jianning Dong, *Senior Member, IEEE*, Belkassem Becetti and Pavol Bauer, *Senior Member, IEEE*

2022 International Conference on Electrical Machines (ICEM) | 978-1-6654-1432-6/22/$31.00 ©2022 IEEE | DOI: 10.1109/ICEM51905.2022.9910702

***Abstract*—This paper investigates a high speed vacuum tube train system relying on wheels for suspension and a multi-mode linear electric machine for charging and propulsion: the machine will be configured as a doubly fed induction machine for charging at stationary, and as a permanent magnet synchronous machine for acceleration and deceleration. The system configuration is first presented, then a linear doubly fed induction machine which can be used for charging at stations is designed and optimized based on genetic algorithm. The design is also validated by finite element modelling. Afterwards, a 1275 km long journey between Damman and Jeddah through Riyadh in Saudi Arabia is selected to demonstrate the application of the presented system.**

***Index Terms*—Linear doubly fed induction machine, high speed railway system, vacuum tube train**

I. Introduction

The transportation sector accounts for 28% of the global energy consumption and nearly a quarter of the global emissions [1]. Decarbonizing of transportation would effectively eliminate the pollution and greenhouse emissions and provide opportunities for the development of high-speed and ultra high-speed ground transportation systems, which have the potential to replace the aeroplanes for long distance travel [2], [3]. Among these systems, the vacuum tube train, or vactrain for short, uses partly evacuated tunnels to reduce the air resistance so that the train can reach higher speed with reduced power consumption. Passengers would sit inside a pressurized pod at atmospheric pressure. The pods travel at very high speed inside the evacuated tubes or tunnels with relatively less power consumption, driven by either rotational or linear motors.

The Hyperloop projects developed based on the vacuum tune train concept usually use magnetic or air levitation with long-stator linear motors to provide the thrust for propulsion and cruising, which increases the system cost. A wheel-based approach is proposed in [4], where a multi-mode linear machine is used for charging, acceleration and deceleration, and a pod side small rotating induction machine is used to provide cruising thrust. Although [4] shows the proposed concept can reduce the system cost and the energy consumption significantly analytically, the design of the multi-mode linear machine was not fully established.

J. Dong and P. Bauer are with the Department of Electrical Sustainable Energy, Delft University of Technology, 2628CD Delft, The Netherlands (e-mail: j.dong-4@tudelft.nl, p.bauer@tudelft.nl).

B. Becetti is with Philips, Eindhoven, The Netherlands (e-mail: belkassem.becetti@gmail.com)

This paper adopts the system design from [4], and investigates particularly at the design of the multi-mode linear machine to demonstrate its feasibility. The system configuration and design constrains are first presented in Section II. Then an analytical design and optimisation approach is given in Section III. Section IV presents the final design and evaluates its performance. Afterwards, the optimised machine will be used in Section V for a case study in Saudi Arabia. Then Section VI concludes the paper.

II. Investigated Vacuum Tube Train System

A. System Configuration

The investigated vacuum tube train system is proposed in [4]. The system configuration is shown in Figure 1. Compared to conventional Hyperloop concept such as the one proposed in [3], the pod is active and has battery as power source for propulsion and cruising. A rotating induction machine with its drive are used to drive the wheels for cruising or emergency drive. There is a three-phase ironless short-stator coil assembly installed under the pod (pod winding). The track system is divided into three sections:

1) Station section: three-phase double-sided iron-core winding (shore winding), which forms a linear doubly-fed induction machine with the pod winding and can be used to charge the battery when the pod is braked (slip $s = 1$).
2) Acceleration/deceleration section: passive track with double sided permanent magnets, which forms a linear synchronous machine with the pod coil. This section is used for launching and regenerative braking.
3) Cruising track: passive track just used for guidance and wheel supporting.

Compared to the Hyperloop concept which requires contactless suspension, this design eliminates the drag caused by electro-dynamic suspension [5] or the high cost laminated track and active control required by the electro-magnetic suspension. However, the top speed might be limited because of the wheel slip and wearing.

B. Design Specifications

Key dimensions and design requirements are based on the data given in [4]. Table I summarizes key design specifications of the multi-mode linear electric machine.A 10000 kg weight and 15 meter long pod with 28 passengers is assumed. The electrical power per pod is 1000 kW. Top cruising speed

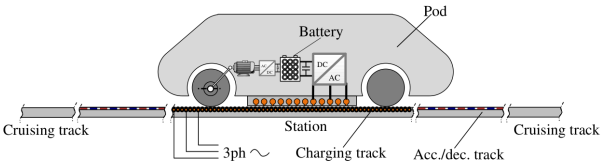

Fig. 1. Wheel based vacuum train system.

is set at $v_{\max} = 700$ km/h. The pod is first charged at 1000 kW at the station, then is launched at a constant acceleration of 1.5 m/s^2 into the acceleration track till the pod power reaches the maximum. Then the pod is further accelerated with a constant power to the cruising speed.

TABLE I
KEY DESIGN SPECIFICATIONS

Item	Value	Unit
Pod power	1000	kW
Pod length	15	m
Max Thrust	15	kN
Shore frequency	333	Hz
Pod frequency	-333 to 970	Hz
Winding height	0.15	m
Pole pitch τ	0.1	m
Mechanical clearance d	1	mm

The frequency of charging at the station is set at 333 Hz, which is the same as the frequency of the transition point between constant thrust acceleration and constant power acceleration.

A mechanical clearance d on both sides is need to separate the shore and the pod assemblies. For the charging section, it is set as low as 1 mm to obtain the smallest possible air gap and reduce the required magnetizing current [6] for the doubly-fed induction machine. However, for the acceleration/deceleration section with permanent magnets and the cruising section, the clearance could be made larger.

III. Design and Optimisation of the Linear Doubly-Fed Induction Machine

A. Key Design Choices

The linear doubly-fed induction machine for the charging section at the station is first designed. The structure and key dimension definitions of the linear doubly-fed induction machine is shown in Figure 2. Based on what has been summarized in Section II, several key design choices can be made. First, based on the pole pitch $\tau = 0.1$ m, it is reasonable to choose the number of slots per pole per phase of the shore winding as $q = 2$. This way it results in a shore side slot pitch of about $\tau_s = 16.7$ mm, which gives a good mechanical property and manufacturability. Then a double-layer short-pitch winding can be chosen for the shore side assembly. The coil pitch is set as five slots to suppress the 5th and 7th harmonics. An open slot laminated iron core is chosen since the equivalent air gap would be large considering the thickness of the pod winding. To limit the iron loss caused by relatively high operation frequency, 0.2 mm thick silicon iron sheet 20WTG1500 from Baosteel or similar core material can be used for the shore core.

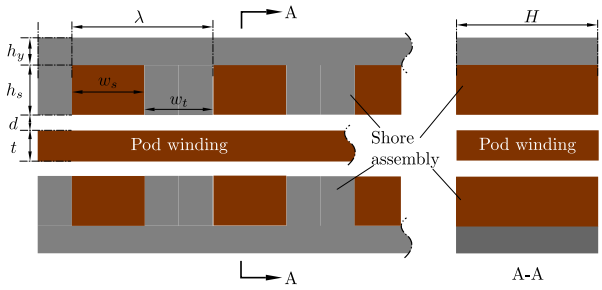

Fig. 2. Key dimensions of the linear doubly fed induction machine.

The pod assembly has an air-core configuration. There are two types of winding configurations it can choose: the overlapped and non-overlapped [7]. In order to have a higher winding factor, so that higher power factor and better possible performance is achieved, the overlapped winding is chosen. The winding distribution of the pod winding is shown in Figure 3. The span of each phase coil side is $\theta_c = 60$ electrical degree. The winding function approach is used to calculate the harmonic winding factors of the chosen winding configuration. The winding function of the pod winding is obtained from the turns counting function by subtracting the average of it. Then the harmonic winding factors are obtained from its Fourier series [8].

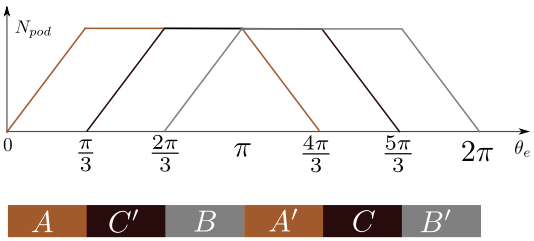

Fig. 3. Pod winding configuration. Top: the turns counting function; Bottom: winding distribution shown as current sheets.

The number of turns per slot of the shore side is chosen as $N_{shore} = 2$ considering the double-layer configuration, and that for the pod side is chosen as $N_{pod} = 1$. Considering the double-sided configuration, the number of the parallel paths of the shore winding is $a = 2$, and the pod winding only has one current path. In this paper the voltages of both sides are not constrained. In practice, the number of turns can be tuned to fit the required voltage and current levels.

The equivalent circuit of the linear doubly-fed induction machine is shown in Figure 4. To minimize the pod side charging AC/DC converter, it is assumed to be controlled to achieve a unity power factor, so that the AC/DC converter can be replaced with a equivalent resistance R_{conv} in the equivalent circuit. Therefore, the charging power at stationary ($s = 1$) is

$$P_2 = 3I_2^2 R_{conv} = 1000 \text{ kW}. \quad (1)$$

where I_2 is the pod side phase current as shown in the equivalent circuit. R_{conv} would also be a design parameter during the machine design and optimisation procedure, and in practice it should be scaled according to the real number of turns of the windings.

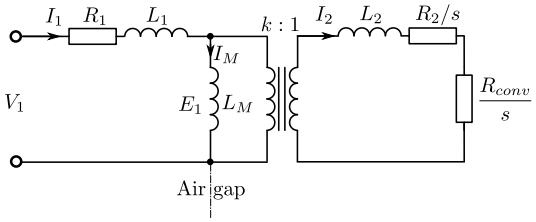

Fig. 4. Per-phase equivalent circuit model of the linear doubly-fed induction machine. An ideal transformer is placed in the middle to address different equivalent number of turns for the shore and pod windings, and the pod side AC/DC converter is modelled as an equivalent resistance R_{conv}.

The turns ratio k in Figure 4 is calculated from the equivalent number of turns by taking the fundamental component of the winding functions [9].

$$k = \frac{N_{sshore} k_{wshore}}{N_{spod} k_{wpod}} \tag{2}$$

where N_{sshore} and N_{spod} are the number of turns in series per phase of the shore winding and the pod winding respectively, k_{wshore} and k_{wpod} are their fundamental harmonic winding factors.

B. Design and Optimisation Procedure

Design of induction machines usually starts with sizing equations based on assumptions of air-gap shear stress σ, or line current density A and air gap flux density B, then work backwards to choose specific dimensions shown in Figure 2 and verify the performance [9], [10]. Several iterations might be needed to reach the final design.

This paper adopts the forward design procedure: equivalent circuit parameters are first identified from geometrical parameters, then the performance of the linear induction machine is evaluated at the required power.

1) Equivalent Circuit Parameters: An analytical approach is used to calculate the equivalent circuit parameters from geometrical design parameters. The iron is assumed to be unsaturated and infinitely permeable. Since the relative permeability of the pod winding is almost 1, the total mechanical air gap length would be the sum of the pod winding thickness t and the mechanical clearance d, as shown in Figure 2:

$$g_m = t + 2d. \tag{3}$$

Assuming an open slot configuration on the shore side, Carter's coefficient K_c given in [6] should be applied to consider the increased equivalent magnetic air gap length g_e caused by the slot openings.

$$g_e = K_c g_m. \tag{4}$$

Assuming a sinusoidal air gap flux density distribution, the magnetising inductance in Figure 4 is calculated as

$$L_M = \frac{6\tau}{\pi^2 p g_e} \mu_0 H (k_{wshore} N_{sshore})^2, \tag{5}$$

where p is the number of pole pairs, H is the coil height as shown in Figure 2.

The shore side leakage inductance is calculated by

$$\begin{aligned} L_1 = &\frac{4\mu_0}{pq}[(\lambda_{slot} + \lambda_{diff})H \\ &+ \lambda_{end} l_{endshore}] N_{sshore}^2, \end{aligned} \tag{6}$$

where λ_{slot}, λ_{diff} and λ_{end} are the coefficients for slot leakage, differential leakage and end-winding leakage respectively [9], $l_{endshore}$ is the turn end length of the shore winding.

Because of the air-core nature of the pod winding, there is no slot leakage. The differential leakage and end winding leakage can be addressed in a similar way as the shore winding, which turn out to be negligible because of the large air gap length.

$$L_2 \approx 0. \tag{7}$$

The shore side and pod side resistances R_1, R_2 are calculated from the active turn length and the end turn length considering the skin effect and proximity effect [11].

Once the iron loss can be obtained from the flux density in the teeth and yoke using the material property [10]. The eddy current loss caused by the air gap field in the pod coil can be calculated the same way as the external proximity effect loss in [11].

2) Design procedure: Based on the above equivalent circuit parameters, the machine performance is solved. Then a genetic algorithm implemented in MATLAB is used to solve the Pareto fronts within the selected geometrical and performance constraints and the targeted optimisation objectives. Constraints are set on the air gap flux density, core flux density and coil current density because they are related to the core material saturation and heat dissipation. Optimisation objectives are set as shore side power factor, pod side coil weight and efficiency.

IV. Optimised Design and Finite Element Method Validation

A. Optimized design

A Pareto front of total loss vs. pod winding weight is obtained after the optimisation, as shown in Figure 5. It can be seen that the machine loss first decreases as weight reduces, however, after the loss reaches 80 kW, any decrease in loss will increase the weight significantly. The machine power factor does not vary significantly throughout the Pareto front, so it is not shown here. In the end a design around the turning point of the Pareto front is selected to achieve a trade-off between the machine efficiency and the weight.

The machine parameters of the select design is shown in Table II. It can be seen that although the efficiency is

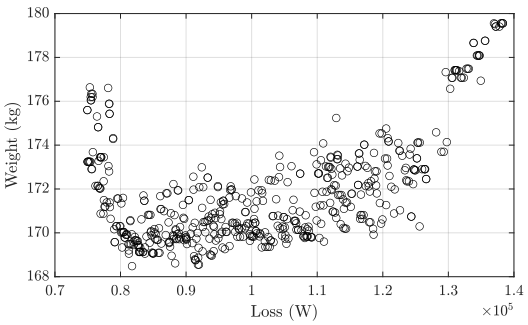

Fig. 5. Pareto front of loss vs. pod winding weight obtained from for the linear doubly-fed induction machine.

acceptable, the power factor of the machine is quite low compared to rotating induction machines, which is because of the large air gap length and agrees with the example linear induction machine design for urban vehicles given in [6].

TABLE II
MACHINE PARAMETERS OF SELECTED DESIGN

Item	Value	Unit
Shore slot opening w_s	10.4	mm
Shore slot height h_s	20.1	mm
Shore tooth width w_t	5.8	mm
Shore back iron height h_y	8.5	mm
Pod coil thickness t	8.2	mm
Pod winding mass	169.5	kg
Shore power factor	0.41	N/A
Efficiency	97%	N/A

Then the same pod winding can be used together with a permanent magnet track for acceleration/deceleration. Assuming the same peak air gap flux density of the linear synchronous machine is the same as that for the doubly-fed induction machine ($B_g = 0.25$ T), the required pod side current is calculated, which is comparable to the charging pod current. If the equivalent air gap length g_e is kept the same, for a permanent magnet with remanent flux density B_r and a relative permeability μ_r, neglecting fringing and leakage, assuming a unit pole arc to pole pitch ratio, the air gap flux density would be

$$B_g = \frac{2h_M B_r}{2h_M + \mu_r g_e}, \tag{8}$$

where h_M is the thickness of the permanent magnets. Therefore, 2 mm thick rare-earth permanent magnets with remanent flux density of 1.0 T should be deployed on both sides to form the acceleration/deceleration track. In practice, the thickness would be larger to counteract the leakage and prevent demagnetisation. Here detailed design will not be given.

B. Finite Element Method Validation

The finite element method (FEM) based procedure outlined in [12] is used to validate the analytical method based design. First the solved magnetising current from the equivalent circuit I_M is applied to the shore side three phase winding, while the pod winding is left open, the peak fundamental air gap flux density B_{g1} is then solved by applying Fast Fourier Transformation (FFT) to the air gap flux density. The magnetising inductance is then calculated as

$$L_M = \frac{2B_{g1}\tau H k_{wshore} N_{shore}}{\sqrt{2}\pi I_M}. \tag{9}$$

The shore winding flux linkage is solved from the same simulation. After applying $\alpha\beta$ transformation to both three phase currents and flux linkages, the shore side main inductance is calculated

$$L_\alpha = L_\beta = \frac{\lambda_\alpha}{i_\alpha}. \tag{10}$$

where L_α and L_β are the main inductances on the α and β axes, which should be equal because there is no saliency. i_α and λ_α are the α axis current and flux linkage respectively. The shore side leakage inductance is then calculated as

$$L_1 = L_\alpha - L_M. \tag{11}$$

The FEM simulated no-load flux density distribution is shown in Figure 6. It can be seen that the shore iron core is not saturated,

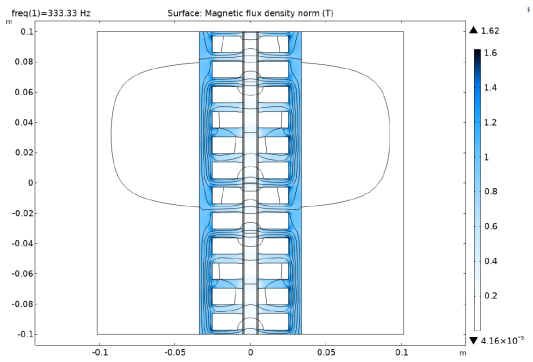

Fig. 6. FEM solved magnetic flux density distribution at no-load condition: magnetising current is applied on the shore side. A single pole-pair is simulated.

Similarly the pod side magnetising inductance L'_M and leakage inductance L_2 can be solved by applying the magnetising current I'_M on the pod side and leave the shore side winding open. Then the transformation ratio k can be solved as

$$k = \sqrt{\frac{L_M}{L'_M}}. \tag{12}$$

Table III compares the main machine parameters and performance obtained from the analytical method and FEM. It can be seen that the analytical design method has reasonable accuracy.

V. CASE STUDY

A. Journey and System Specifications

A journey between cities of Dammam and Jeddah via the capital city Riyadh in the Kingdom of Saudi Arabia shown in

TABLE III
COMPARISON OF PARAMETERS FROM ANALYTICAL METHOD AND FEM

Item	Symbol	Analytical	FEM	Unit
Air gap flux density	B_{g1}	0.26	0.25	T
Magnetising inductance	L_M	1.1	1	mH
Shore leakage inductance	L_1	151	135	μH
Pod leakage inductance	L_2	0	8	nH
Transformation ratio	k	1.95	1.97	N/A
Loss	p	72.5	80	kW

Figure 7 is used to benchmark the multi-mode linear electric machine based system studied in the paper and the Hyperloop system described in [3].

Fig. 7. Studied journey for the vacuum tube train system.

The specification of the Hyperloop system is obtained from [3], while the specification of the system investigated in the paper is from [4] and the propulsion relies on the machine designed in Section IV. For the investigated system, the specific energy density of the on-board battery is set as 200 Wh/kg, while the battery mass to pod mass ratio is set as 12%. Table compares the other key specifications.

TABLE IV
SPECIFICATIONS OF BOTH SYSTEMS: HYPERLOOP VS. INVESTIGATED SYSTEM

Item	Investigated	Hyperloop
Passenger capacity per pod	28	28
Pod payload (kg)	10000	15000
Cruising speed (km/h)	700	1000
Launch mode	Constant power	Constant acc.
Max. acceleration (m/s^2)	1.5	4.9
Rated power (MW)	1	21
Acceleration distance (km)	22.7	7.9
Acceleration time (min)	3:30	0:57
Mass active track coil (kg/m)	68.7	800
Suspension system	Wheels	Air bearing
Cruising power (kW)	100	364

B. Benchmarking

The following assumptions are made for the simulation of the journey:

1) Initial state of charge (SOC) of the on-board batteries in the investigated system is 20%;
2) Charging at stations can occur while passengers are disembarking/embarking;
3) Most and if not all of the kinetic energy gained during launch is recovered during deceleration;
4) All non-propulsion loads are the same;
5) Both systems spend the same amount of time at stations between journeys.

Based on the above assumptions, a MATLAB script is made to simulate the complete journey. The speed, thrust, specific power and state of the charge of the battery of the investigated system is obtained and plotted in Figure 8. It shows that the battery SOC is always between 20% and 90% which proves the sizing of battery is properly done.

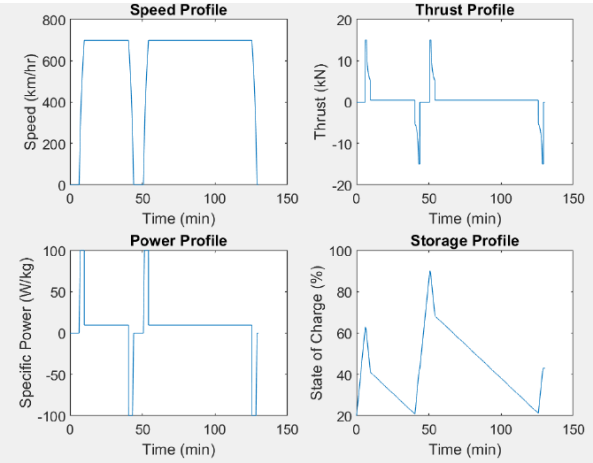

Fig. 8. Journey profiles for the investigated system.

The simulated speed and specific power profile of the two system is compared in Figure 9. It can be seen that because of the limit of wheel based propulsion system, the investigated system reaches a lower cruising speed and thereby requiring more time to complete the entire journey. However, it requires a much less peak power during the acceleration and deceleration phases, which leads to significantly less costly electrical infrastructure. The air bearing system required by the Hyperloop pod for suspension and cruising results in a higher energy consumption as compared to the investigated system, as shown in Table V.

TABLE V
JOURNEY TIME AND ENERGY CONSUMPTIONS OF THE TWO SYSTEMS

Item	Investigated	Hyperloop
Time consumption (h)	2:03	1:25
Energy consumption (Wh/km/pass.)	4.5	17

VI. CONCLUSION

This paper investigated an alternative vacuum tube train concept which relies on wheels and a multi-mode linear electric machine for suspension. Optimal design of the machine

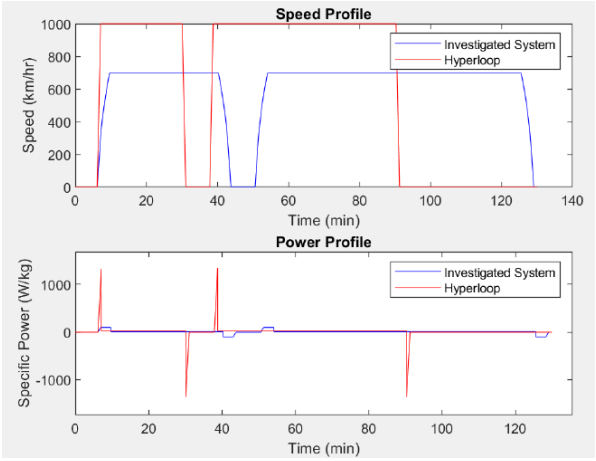

Fig. 9. Speed and specific power profiles for the two systems.

has been implemented based on the analytical method and multi-objective optimisation. Based on the designed machine, the investigated concept has been benchmarked against the original Hyperloop concept, showing a significant reduction in energy consumption.

VII. References

[1] P. C. Renske Schuitmaker, Till Bunsen and A. Braschi, "Railway Handbook 2017 – Analysis," International Energy Agency, Tech. Rep., 2017. [Online]. Available: https://www.iea.org/reports/railway-handbook-2017

[2] V. Smil, "The hyperloop is hyper old: Elon musk merely renamed a 200-year-old dream: Numbers don't lie," *IEEE Spectrum*, vol. 58, pp. 18–19, 2021.

[3] E. Musk, "Hyperloop Alpha," Tesla Inc., Tech. Rep., 2013. [Online]. Available: https://www.tesla.com/sites/default/files/blog_images/hyperloop-alpha.pdf

[4] A. Veltman, P. van der Hulst, M. Jonker, and H. Polinder, "Tunnel-Vision on Economic Linear Propulsion?" in *2019 12th International Symposium on Linear Drives for Industry Applications (LDIA)*, Jul. 2019, pp. 1–6.

[5] M. Flankl, T. Wellerdieck, A. Tüysüz, and J. W. Kolar, "Scaling laws for electrodynamic suspension in high-speedtransportation," *IET Electric Power Applications*, vol. 12, no. 3, pp. 357–364, 2018, _eprint: https://onlinelibrary.wiley.com/doi/pdf/10.1049/iet-epa.2017.0480. [Online]. Available: https://onlinelibrary.wiley.com/doi/abs/10.1049/iet-epa.2017.0480

[6] I. Boldea, *Linear Electric Machines, Drives, and MAGLEVs Handbook*. CRC Press, 2013.

[7] A. Mohammadpour, A. Gandhi, and L. Parsa, "Winding factor calculation for analysis of back EMF waveform in air-core permanent magnet linear synchronous motors," *IET Electric Power Applications*, vol. 6, no. 5, pp. 253–259, May 2012.

[8] T. A. Lipo, *Analysis of Synchronous Machines*. CRC Press, Dec. 2017.

[9] J. Gieras, *Linear Induction Drives*. Oxford University Press, Jan. 1994.

[10] J. Pyrhonen, T. Jokinen, and V. Hrabovcova, *Design of Rotating Electrical Machines*, 2nd ed. Wiley & Sons, Ltd, Oct. 2013.

[11] J. Mühlethaler, "Modeling and multi-objective optimization of inductive power components," Doctoral Thesis, ETH Zurich, 2012.

[12] J. Nerg, J. Pyrhonen, and J. Partanen, "Finite element modeling of the magnetizing inductance of an induction motor as a function of torque," *IEEE Transactions on Magnetics*, vol. 40, no. 4, pp. 2047–2049, Jul. 2004.

VIII. Biographies

Jianning Dong received the B.S. and Ph.D. degrees in electrical engineering from Southeast University, Nanjing, China, in 2010 and 2015, respectively. Since 2016, he has been an Assistant Professor with the DC System, Energy Conversion, and Storage (DCE&S) Group, Delft University of Technology (TU Delft), Delft, The Netherlands. Before joining TU Delft, he was a Postdoctoral Researcher with McMaster Automotive Resource Centre, McMaster University, Hamilton, ON, Canada. His research interests include electromechanical energy conversion and contactless power transfer.

Belkassem Becetti is an Algerian national born on February 5th, 1997. He received his Bachelor of Science (B.Sc) degree, in the field of Electrical Engineering, from Texas A&M University in 2019. He completed his Master of Science (M.Sc) degree in Electrical Engineering, with a specialization in Power Electronics and Electrical Machines from the Delft University of Technology in 2021. During his studies, his research interests were the control of electric drives and the design of electrical machines. Recently, he moved to Eindhoven in the Netherlands in pursuit of his dream of becoming a Mechatronics specialist in the high-tech industry

Pavol Bauer received the master's degree in electrical engineering from the Technical University of Kosice, Kosice, Slovakia, in 1985, and the Ph.D. degree from the Delft University of Technology, Delft, The Netherlands, in 1995. He is currently a Full Professor with the Department of Electrical Sustainable Energy, Delft University of Technology, where he is the Head of DC Systems, Energy Conversion and Storage Group. He has authored or co-authored 72 journals and almost 300 conference papers (with H factor Google scholar 43, Web of Science 20) and 8 books, and holds 4 international patents. He has organized several tutorials at the international conferences. He has worked on many projects for industry concerning wind and wave energy, power electronic applications for power systems such as Smarttrafo; HVdc systems, projects for smart cities such as PV charging of electric vehicles, PV and storage integration, contactless charging; and he has participated in several Leonardo da Vinci and H2020 EU projects as project partner (ELINA, INETELE, E-Pragmatic) and coordinator (PEMCWebLab.com-Edipe, SustEner, Eranet DCMICRO). Dr. Bauer was a recipient of the title Prof. from the President of Czech Republic at the Brno University of Technology in 2008 and the Delft University of Technology in 2016.